Green Chemistry

Size-tailorable Lignin Nanoparticle Synthesis: Effects of Solution Chemistry and DLVO Forces on Amphiphilic Balance of Lignin

Journal:	*Green Chemistry*
Manuscript ID	GC-ART-05-2023-001871.R2
Article Type:	Paper
Date Submitted by the Author:	23-Sep-2023
Complete List of Authors:	Li, Qianwei; University of Missouri Zhang, Hanwen; University of Missouri, Lee, Jaewon; University of Missouri Wan, Caixia; University of Missouri, Biomedical, Biological, and Chemical Engineering

Size-tailorable Lignin Nanoparticle Synthesis: Effects of Solution Chemistry and DLVO Forces on Amphiphilic Balance of Lignin

Qianwei Li [a], Hanwen Zhang [a], Jaewon Lee [b, *], Caixia Wan [a, *]

[a] Department of Chemical and Biomedical Engineering, University of Missouri, 1406 East Rollins Street, Columbia 65211, USA

[b] Department of Mechanical and Aerospace Engineering, University of Missouri, 416 South 6th Street, Columbia 65211, USA

*Corresponding author. Tel: +1 573 884 8918; E-mail: j.lee@missouri.edu. Tel: +1 573 884 7882; E-mail: wanca@missouri.edu.

Abstract

Lignin nanoparticles (LNPs) have gained great interest for a promising renewable nanomaterial toward value-added applications. This work investigated solution chemistry and particle-particle interaction force in the LNP formation aiming at a facile technique to balance amphiphilic properties of lignin for size-controlled synthesis. By facilely tuning solution chemistry, lignin with different amphiphilic properties can form the nanoparticles with 57-262 nm and dispersity index (Đ) less than 0.2 at an initial lignin concentration of 10-80 g/L. A numerical estimation of particle size was established with Derjaguin-Landau-Verwey-Overbeek's (DLVO) theory and population balance equation (PBE) to evaluate the interaction energy of particles as the function of solution chemistry and lignin properties. In the developed DLVO-PBE model, lignin properties such as molecular weights and content of functional groups are closely related to the repulsive energy calculation in the particle collision and further determine the assembly patterns. The model can be applied to lignin with varied properties with high prediction accuracy, especially in the DLVO forces-driven aggregation. It also suggests that solvated lignin chains can involve the uneven electrostatic force field and non-

DLVO forces leading to a broad/multi-modal size distribution. Overall, the combination of experimental and theoretical investigations provides new insights into assembly mechanisms of lignin molecules involved in the formation of nano-/submicron particles.

Keywords: Lignin nanoparticles, DLVO forces, population balance modeling, amphiphilic balance, self-assembly

1. Introduction

Lignin is a naturally occurring aromatic polymer with abundant functional groups, possessing attributes such as anti-UV, antioxidant, and antimicrobial activities. Despite great potential for broader applications, its inherent heterogeneity and poor solubility in aqueous solutions limit its overall effectiveness in higher value-added uses. Engineering lignin into nano- or sub-micrometer particles would potentially address those limitations especially by offering additional molecular interactions capabilities.[1] For example, engineered nanoparticles would exhibit improved stability due to enhanced π-π stacking interactions and also engage in selective interactions with external molecules, being facilitated by increased surface hydrophilicity and electrostatic forces.[2, 3] Organic fractionation or surface functionalization can lead to lignin with modified chemistry such as hydrophilicity/hydrophobicity yielding LNPs with desired attributes.[4, 5] Lignin nanoparticles (LNPs) have relatively uniform particle sizes ranging from 20 to several hundred nanometers and can be achieved via self-assembly of lignin.[6] LNPs as natural nanomaterials become a promising candidate for drug carriers, UV blockers, Pickering emulsion stabilizers, etc., and have found uses in biomedical, agricultural, and environmental fields.[7, 8] For example, incorporating LNPs especially with smaller sizes into functional materials can improve antibacterial activities. Technical lignin, such as kraft lignin (KL) and organosolv lignin (OL),[9-11] has been used for LNP synthesis due to commercial availability and low cost. Antisolvent method is classically adopted to trigger the nucleation-

growth/adsorption of lignin for self-assembly.[11-14] LNP properties, especially particle size and morphology, depend on several key factors including lignin chemistry,[15-18] solvent type,[19] antisolvent mixing rate,[20] and initial lignin concentration.[21] Thus, it is important to elucidate the process-structure relationship of lignin assembly for tailoring morphology and size of LNPs suited to various applications including emerging areas like drug delivery and soft materials in physiological systems.

Molecular interactions involved in lignin self-assembly are largely determined by hydrophilic (e.g., hydroxyl and carboxyl groups) and hydrophobic (e.g., aromatic, acetylated) groups in lignin. Prior studies in LNP formation focused on lignin property-orientated mechanisms. For example, lignin with high molecular weights but low contents of hydrophilic groups would result in small nanoparticles due to low lignin-water interactions.[22] Besides, low phenolic hydroxyl and high aliphatic groups are also reported as contributing factors for small particles sizes.[13, 17] Electrostatic forces are essential to overcome attractive interactions and slow down the particle growth. The aggregation kinetics driven by interaction energy would eventually determine the size profile of polymer aggregation.[23] Therefore, it is important to study the effects of lignin chemistry on LNPs synthesis because it can fundamentally determine interaction forces between lignin chains. Recently, lignin valorization involving fractionation, depolymerization, and/or functionalization have also been extensive studied, and the involved mechanisms and kinetics also elucidated.[24-27] Those valorization approaches can be integrated with LNP production by endowing lignin with new functionality or amphiphilic balance offering a more powerful platform for property-tailorable LNPs synthesis. To this end, it is crucial to study lignin chemistry and its relation to lignin self-assembly kinetics and subsequent properties including nanoparticle size. Therefore, the research in this regard represents a critical area of focus for promoting the mass production of LNPs with desired attributes for downstream valorization.

Lignin self-assembly mechanisms previously reported are mainly based on the assumption that lignin properties especially initial structures govern its assembly behavior upon antisolvent (mostly water) addition. However, this assumption neglects possible antisolvent effects on lignin molecular interactions, and an explicit connection between initial conditions and aggregation termination remain unclear. To fill this gap, we hypothesized that size-tailoring can be achieved via rearranging surface hydrophilic groups of lignin during the assembly, to be specific, tunning the chemistry of solution where lignin aggregation takes place. When the well-defined nanospheres are formed, it requires strong π-π stacking to stabilize the hydrophobic core and sufficient repulsive force to prevent further aggregation.[28] The mutual factors of molecular interactions and repulsive forces are ionizable hydrophilic groups (i.e., phenolic hydroxyl and carboxyl groups) in lignin. The ionization of those hydrophilic groups can not only provide more negative charges but also interrupt molecular interactions and rearrange surface hydrophilic groups, ultimately lignin structures. Controlling hydrophilic groups' ionization would thus provide a potential strategy to synthesize nanoparticles from lignin with more hydrophobicity or in high concentration where lignin tends to aggregate fast.

A precise size-tailoring platform can be achieved via coupling theoretical/computational modeling with experiments. Few prediction models for particle sizes of soft materials have been developed based on a self-consistent field theory combined with density functional theory or data-driven modeling.[29, 30] Prior studies proposed the plausible relationship between lignin properties and LNPs size qualitatively,[4, 13, 17, 19, 31, 32] but did not provide a numerical size estimation method. The challenge of modeling lignin in the prior studies lies in its complex structure. For example, various functional groups and randomly entangled chains with electrostatic effects between or within chains can introduce additional complexity compared to polymer with repetitive units or defined chemical structures. Since repulsive forces are key to reduce aggregation, its calculation based on the ionizable group

content of lignin can advance the understanding of effects of lignin properties on particle sizes. Herein, we first investigated the LNP formation based on the Derjaguin-Landau-Verwey-Overbeek's (DLVO) theory for the interactions in colloidal dispersions,[33] with the assumption that each lignin chain can be approximated as a spherical particle due to self-aggregation of hydrophobic part. Once one LNP attaches with another, the LNPs can become nucleated and grown. The modeling of DLVO for LNPs provides their energetics quantitatively by a delicate balance/correlation between van der Waals and electrostatic forces which are influenced by detailed chemical physics at a molecular level.[33, 34] In the meantime, the energetic studies (DLVO) can expand to the kinetics of LNP growth mechanisms by incorporating von Smoluchowski's population balance equation (PBE).[35] Since the effects of detailed chemical physics are correlated with the integrated DLVO and PBE (DLVO-PBE), the self-consistency can be established via the coupling of theoretical calculations with experimentation.[36-38]

In this study, we first quantified the chemical structures of lignin (with emphasis on the ionizable groups like phenolic hydroxyl and carboxyl groups) and molecular weight and revealed their effects on particle size distribution. Solution chemistry was adjusted under weak acid/base conditions and at different salt concentrations for LNP synthesis. The DLVO-PBE model was then developed to understand growth mechanisms of LNPs according to lignin characteristics and solution chemistry. The developed model was applied to demonstrate energy barrier change and predict particle size distribution under different conditions including initial lignin concentrations, solution pH, and salt concentrations. We proposed that surface ionizable group density (especially carboxyl groups) is the critical parameter to determine the involvement of lignin chains and is highly affected by the LNP synthesis methods and LNPs themselves. The solution chemistry tuned by formulating the antisolvent changes lignin structure and the availability of surface ionizable groups, which can be applied to all the studied lignin types. To the best of our knowledge, this work was for the first time to establish the

energy profile of the lignin particle-particle interactions and further apply it to the size prediction.

2. Synthesis of lignin nanoparticles

LNPs were formed by rapidly mixing a freshly prepared antisolvent with lignin solution at 3:1 mass ratio with vigorous agitation at room temperature for 15 min. Lignin solution was prepared by dissolving a lignin sample at 10-60 g/L in 68% aqueous acetone solution. Antisolvent with pH 5-8.5 and 0-50 mM salt/electrolyte was prepared using either ammonium chloride (NH_4Cl) or ammonium bicarbonate (NH_4HCO_3). The suspension was transferred to a dialysis bag (MWCO 14000, Fisher Scientific (Waltham, MA)) and washed in deionized (DI) water to remove residual acetone and inorganic salts. The particles were measured at 48 h after assembly. The characterization of LNPs was described in Supporting Information.

3. Theoretical calculations in DLVO-PBE model

Lignin–lignin interaction forces can be described quantitatively by the DLVO theory. In this theory, the interaction forces (F^{DLVO}) is contributed by attractive van der Waal forces (F^{vdW})[39] and repulsive electrostatic force (F^{elec}):[40]

$$F^{DLVO} = F^{vdW} + F^{elec} \#(1)\#$$

We first calculated the DLVO forces for the interaction between two plates (denoted as F_{PP}) using **eq 2 and 3.** It should be noted that **eq 3** originates from a charge-regulation model by Ninham and Parsegian [41] which is the combination of the non-linear Poisson-Boltzmann equation and the fraction of dissociated ionizable surface groups.

$$F_{PP}^{vdW} = -\frac{A_H}{6\pi D^3} \#(2)$$

D is the distance between two plates. A_H ($= 17\ zJ$) is the Hamaker constant of lignin-water-lignin determined by Lifshitz theory.[34]

$$F_{PP}^{elec} = nk_BT\left[\xi - 1 + \left(\frac{1}{\xi} - 1\right)\left(1 - \frac{\eta}{2}\right) + \frac{\left(\frac{1}{\xi^2} - 2\right)\eta}{2}\right] \#(3)$$

Where n is the number of total anions, k_B is the Boltzmann constant and T (=298 K) is ambient temperature. For a negatively charged surface, when only monovalent cations are present, $\eta = 0$, and if only divalent cations are included, $\eta = 1$. ξ as the reduced potential at the center between two plates is the function of the area per surface ionizable group (S), dissociation constant of ionizable group (H), solution pH, Debye length (κ) (more details included in Supporting Information).

The particle-particle interaction force and energy calculation can be obtained via applying the Derjaguin approximation numerically [42] on the plate-plate interaction energy calculation. The PBE was further determined as the difference between the numbers of the newly generated particles and particles consumed in the aggregation toward larger particles:[37, 38, 43]

$$\frac{dn_k}{dt} = \frac{1}{2}\sum_{i+j=k}\beta_{ij}n_in_j - n_k\sum_{i=1}^{\infty}\beta_{ik}n_i \#(4)$$

Where β_{ij} is an aggregation kernel which is related to the energy profile of the particle-particle interaction calculated above (more details included in Supporting Information).

4. Results and Discussion

4.1. Effects of lignin properties on the LNP formation

Lignin properties, mainly ionizable functional groups and molecular weights, were studied for their effects on the LNP formation. Three types of lignin (i.e., kraft lignin (KL), organosolv lignin (OL), and ethanol soluble lignin (EKL)), which are commonly reported as starting materials for value-added lignin application,[44] were studied covering a reasonable range of ionizable functional group contents and molecular weight distributions. As

summarized in **Table 1**, KL had 14% and 41% higher phenolic groups than OL and EKL, respectively. The carboxyl group content followed the order of KL < EKL < OL, while the phenolic hydroxyl group content had the opposite. All the three lignin samples had higher phenolic hydroxyl groups than the carboxyl groups and showed more variations in the number of phenolic hydroxyl groups (~1) than that of aliphatic hydroxyl groups. For molecular weight distribution, KL had 27% and 51% bigger Mw than OL and EKL.

In addition to ^{31}P NMR analysis, the ionization UV difference method was also used to further quantify phenolic hydroxyl groups including uncondensed-unconjugated (Type Ⅰ), uncondensed-conjugated (Type II), condensed-unconjugated (Type Ⅲ), and condensed-conjugated (Type Ⅳ) (**Fig. 1a and b**). Type Ⅰ and Ⅱ are ionizable under weak base conditions with a medium pK_a of 9.85-10.27 and a relatively low pK_a of 7.5-8.5, respectively.[45] Partial ionization of phenolic hydroxyl groups (Type I&II) was demonstrated using 20 mM NH_4HCO_3 (detailed in Supporting Information). The results indicated the relation between partial ionization of phenolic hydroxyl groups and lignin structure. For example, an extended structure increases the availability of ionizable groups on the particle surface, which contributes to negatively charged surface of LNPs. Meanwhile, the ionization of phenolic hydroxyl groups interrupts the hydrophobic interaction and hydrogen bonding in lignin, leading to the modification of lignin structure.

Both weak base and weak acid conditions (e.g., water as antisolvent) can trigger the lignin aggregation. Different pH can influence the ionization of hydrophilic groups (carboxyl and Type I and II phenolic hydroxyl groups), which further alters the assembly behavior of lignin molecules. The tuning effect of weak base conditions also reflects on the changes in the F^{elec} of the particles endowed by the surface ionizable groups. Herein, DLVO force calculation was performed to evaluate the contribution of carboxyl and phenolic hydroxyl groups to the F^{elec}. Within a pH range of 3-8, the low dissociation constants of phenolic hydroxyl groups

(pK$_a$ = 7.5 or 10.2) suggest a considerably low amount of such functional groups being ionized compared to carboxyl groups. It can be expected that phenolic hydroxyl groups cannot contribute much to the repulsive force in particle-particle interactions. The particle-particle interaction energy profile at different pH proved the main contribution by carboxyl groups in total energy (**Fig. S4, as detailed in supporting information**). It is validated that the energy depth is mainly attributed to the carboxyl groups while the additional phenolic hydroxyl groups would only increase the F^{elec} by a small quantity. For example, at pH 5.3, the energy depth difference between the calculations with or without the inclusion of phenolic hydroxyl groups is only 2.71 kT (**Fig. S4b**). This finding indicated that the carboxyl groups of lignin played a major role in the determination of electrostatic force, as previously reported.[46]

Lignin molecular weight also had significant effects on the LNP size under the same solution chemistry condition. A negative relation between Mw and LNP size was revealed (**Fig. 1c**), which agrees with earlier reports that high molecular weight lignin tends to form small nanoparticles.[13, 17] Higher molecular weight fragments ensure the electrostatic stabilization of the particles with additional repulsion through the interaction of the interpenetrating charged fragments.[47] The resulting aggregates thus consume less lignin chains, forming a small and compact structure.

4.2. LNP size regulation via antisolvent formulation

We focused on the solution chemistry (pH, salt concentration), initial lignin concentration, and lignin property/lignin type for their effects on the LNP formation as those three key experimental factors would determine the particle-particle interaction energy and ultimately LNP size **(Fig. 2)**. The ionizable groups in lignin, including carboxyl groups (pK_a = 4.8) [48] and two types of phenolic hydroxyl groups (Type I at pK_a = 7.5-8.5 and Type II at pK_a = 9.85-10.27), can all contribute to the repulsive forces in the particle collision. In the interaction between two negatively charged particles, the initial lignin concentration (c_{init})

corresponds to the initial separation distance ($D_{average}$) of lignin chains, and the salt concentration relates to the Debye length (κ) of the negatively charged groups. The calculated $D_{average}$ and κ are included in Supporting Information, and the ratio $D_{average}/\kappa$ and κ used for LNP size analysis are referred to c_{init} and salt concentration, respectively. It can provide a better connection between the energy profile and particle growth. It should be noted that the final pH of the mixture is determined by both formulated antisolvent and lignin initial concentration (**Fig. S1**). A weak acid assembly can be simply achieved when DI water is antisolvent and the final pH reduces due to the ionization of lignin functional groups. To further study the salt concentration effect at weak acid condition, 0-13 mM NH_4Cl was added in the antisolvent. KL, OL, and EKL were used in LNP synthesis via directly mixing lignin solution at 10 g/L c_{init} with DI water. KL stood out with the uniform and smallest size (55.93 nm) as revealed by TEM images (**Fig. 3a and b**), while OL/EKL formed oval/gourd and irregular micron-particles (**Fig. S5**). The LNP size of KL further decreased then increased as c_{init} increased from 1 to 50 g/L (corresponding to the separation distance from 28 to 3.5 nm) (**Fig. 4a**). The large particles were formed in the lowest concentration as the tendency of minimizing the surface free energy overcomes the repulsive electrostatic force.[13] A negative exponential relation between Debye length (κ from 30.7 to 2.7 nm) and particle size was observed while keeping the initial separation distance the same (**Fig. 4b**). Particle size distribution with low dispersity index (Đ) was observed in most cases under weak acid conditions (**Fig. S7a and b**).

The shift from weak acid to weak base condition with NH_4HCO_3 solution as the antisolvent led to a different scenario of assembly. All the three lignin types can form spherical particles (**Fig. 3b-d**). Interestingly, the small pores were formed in OL-NPs (insert in **Fig. 3c**) but not in KL-NPs or EKL-NPs. KL-NPs at 10 g/L c_{init} were mainly aggregates with no well-defined shells (**Fig. S6**). The obtained nanoparticles have low Đ (<0.2) following the order of KL < EKL < OL at the same c_{init} except KL-NPs at c_{init} below 20 g/L (**Fig. 4c–e**). The particle

sizes have a positive linear relation with c_{init} (**Fig. 4d and e**), and at the same c_{init} the particles synthesized under weak base condition are smaller than the particles obtained under weak acid condition. ζ potential of the synthesized particles was also measured after removing NH_4HCO_3 via dialysis (**Fig. 4f)**. Surprisingly, the most negatively charged/most stable particles can be obtained even at 30-60 g/L c_{init}. The change in the salt concentration (corresponding to Debye length) resulted in two size distribution profiles of KL-NPs. At 10 g/L c_{init}, the multi-modal/broad distribution (Đ > 0.3) was observed at ≥5 mM NH_4HCO_3 (**Fig. 4c**). At 20 g/L c_{init}, the monodisperse particles (Đ < 0.2) were obtained with at the closer separation distances except at a very high salt concentration (500 mM) (**Fig. S7c and d**).

Based on the LNP size distributions under different conditions, it can be concluded the structure of lignin chains initially defined by their own chemistry can be further modified by solution chemistry, which in turn governs the assembly pattern of lignin chains and final particle size. When the chain attachment reached equilibrium with sufficient F^{elec}, it prevented further aggregation of particles, resulting in smaller sizes. The screening effect of electrolyte predominates the aggregation in weak acid condition but only plays a minor role in weak base conditions.

4.3. DLVO-PBE modeling of collision-driven lignin aggregation

We further employed the DLVO theory-based colloidal dispersion approaches to elucidate lignin assembly. It is our hypothesis that the particle size could be stabilized energetically, which can be determined by the balanced colloidal dispersion forces (including van der Waals force (F^{vdW}) and electrostatic repulsion force (F^{elec}), **eq 1**) and Brownian motions (F^{Br}). There are two main assumptions for modeling that (1) an individual lignin chain or nanoparticle assembled with >2 lignin chains per LNP can be considered as a colloidal particle and (2) the growth of LNPs can occur by particle-particle attachments.

We first examined the energy barrier of interaction of two spherical particles at

different densities of carboxyl groups (inverse of area per ionizable groups), particle size, and size ratios between two particles (**Fig. 5a and b**). The content ratio of phenolic hydroxyl to carboxyl groups, in a particular lignin, was assumed constant in the following calculations. Thus, only the area per carboxyl group (S_{COOH}) in a particle was presented. When the spherical particle size maintains same (with a radius of 24 nm applied here as an example), the energy depth decreases exponentially as S_{COOH} increases from 0.086 to 4.34 nm^2/ion, and attachments of equal-sized particles would be dominated with almost half of the energy barrier for the particles having different sizes (**Fig. 5a**). The selected S_{COOH} range in **Fig. 5b** aims to show the overall trend of the energy depth. Repulsive force increases along with the growth of particles, which can play a crucial role in stabilizing assembled LNP at a certain diameter. The Brownian motion distribution for the particles with a radius of 24 nm was shown in **Fig. 5c**. Depending on the surface ionizable group contents, Brownian motion can overcome the energy barrier leading to the particle attachment. It can also dominate the attachment when the particle radius is smaller than 5 nm with the relatively shallow energy barrier (absolute value < 20 kT) (Insert of **Fig. 5b**).

It is essential to have strong F^{elec} for the particles to prevent further aggregation to maintain small sizes. The screening effect of 0.1-13 mM NH_4Cl can counteract the repulsive barrier of the LNPs, leading to the formation of larger particles. To maintain their stability in an aqueous phase, the lignin particles tend to grow larger and larger until they become energetically stable. In another words, the DLVO forces (the sum of F^{vdW} and F^{elec}) against attachments of lignin can be largely influenced by the electrolyte concentration, and a relatively low force barrier led to increased particle sizes. Therefore, the exponential relations between the hydrodynamic diameter and NH_4Cl electrolyte concentrations (**Fig. 4b**) are aligned with $F^{elec} \sim e^{-\kappa}$, where $D_{average}/\kappa$ ranges from 0.06 to 0.69.

It is concluded based on experiments that salt concentration, pH and lignin types are

the decisive factors to desolvation effect. Because lignin structure changed corresponding to the desolvation degree,[49] it is expected that the ionizable groups content on the lignin surface vary in different pH and lignin types. Under the weak acid condition (pH 2.97-5.25), the S_{COOH} of KL and OL is estimated to be 87.87 and 136.19 Å^2/ion, respectively, as detailed in Supporting Information. A reasonable agreement was achieved for both types of lignin (**Fig. 6a and b**) with the relative errors between 10 to 30 % when the particle size is above 50 nm at an appropriate range of initial lignin concentration. For example, the particle size of LNP dispersed in DI water was predicated to be 57.5 nm (corresponding to 39.9 nm measured) for KL at c_{init} = 3 g/L (**Fig. 6a**) and 70.8 nm (corresponding to 64.9 nm measured) for OL at c_{init} = 1 g/L (**Fig. 6b**).

Under the weak base conditions (pH7-8.3), the predicted particle sizes tend to be smaller regardless of the initial lignin concentration due to substantially improved dissociation on the ionizable groups. In the calculation, the estimated S_{COOH} under such weak-base condition leads to approximately zero surface potential (**Fig. S8**), which suggests unstable state and disagrees with the experimental data (**Fig. 4f)**. It suggests that non-DLVO forces (e.g., π-π stacking interaction) surpassed the total DLVO forces, continuing the aggregation until a stronger repulsion is reached. The S_{COOH} applied to calculate the average particle size under the weak base condition is 682.4 and 1822 nm^2/ion for KL and OL (both at c_{init} = 80 g/L), respectively. Although the predicted sizes at c_{init} = 10-60 g/L under the weak base condition are still underestimated (**Fig. 6c and d**), the gap between the measured and predicted values is getting closer as c_{init} increases. It suggests that DLVO forces take charge again in determining the aggregation kinetics at the crowded particle spacing and lower equilibrium pH. The larger LNP sizes are found in the early stage at the higher initial lignin concentration. It indicated that not only the surface charge density and Hamaker constant of lignin but also the initial separation distance between LNPs at an early stage can play a crucial role in determining the

LNP size via interplaying F^{vdW}, F^{elec}, and F^{Br}.

In the proposed DLVO-PBE model, the size prediction was performed assuming that each particle has the same surface ionizable group density. It should be noted that the dispersity of the lignin chains also plays an important role and can explain the disparity between the calculated and measured sizes. The dispersity of lignin can reflect on its molecular weight distribution which further correlates with the functional group content per lignin molecule.[50] Diverse functional groups in lignin chains and molecular weights led to unevenly distributed F^{elec} fields. It can result in heterogeneous growth of LNPs, such as oriented attachments by unevenly distributed F^{elec} fields, and thus the bimodal or trimodal particle size distribution could appear. One example is the different size distribution at c_{init} = 10 g/L and over 20 g/L under the weak base conditions. At the low lignin concentration ($D_{average}/\kappa$ = 8.5 at c_{init} = 10 g/L), the heterogenous distributions of ionizable groups combined with different degrees of local screening effects caused the significant variations of attachment efficiency across lignin chains. Consequently, a bimodal or even trimodal particle size distribution was observed (**Fig. 4c**). By reducing the initial separation distance ($D_{average}/\kappa$ = 6.8 at c_{init} = 20 g/L), the nullified uneven F^{elec} field resulting from the multi-body interactions or increased collision efficiency reduced the effect of the heterogeneity of chain attachment especially in the latter stage of the collision, thus facilitating the relatively uniform particle formation (**Fig. 4d and S7d**).

Through the estimation of area per ionizable group for a single lignin chain based on reported NMR and GPC data [13, 17, 50, 51], the low or high molecular weight lignin chain can contain more ionizable group content on surface (**Fig. S9**). We further investigated the other factors besides heterogeneity by using fractionated lignin (i.e., AKL with M_w 6017 g/mol by removing small molecular weight fractions) was used in LNP synthesis. AKL-NPs had a particle size of 42.86 nm (Đ = 0.25) when DI water was used as the antisolvent, which agrees with the negative correlation between the size and molecular weight. Synthesized under weak

base conditions, AKL-NPs were compared to the LNPs of EKL (M_w 2705 g/mol) and KL (M_w 5529 g/mol). A multimodal/broad size distribution of AKL-NPs was observed at c_{init} = 10-40 g/L (**Fig. 6e**). The 1st peak of the AKL-NPs size distribution was compared with the predicted size (**Fig. 6f**). Using the same estimated S_{COOH} from KL, a better agreement (relative error of 8-29 %) was achieved than the unfractionated KL (relative error of 34-67 %) expect at c_{init} = 60 g/L. It suggests that our DLVO-PBE model can better predict the assembly of lignin chains with narrow-range, relatively high molecular weight. One the other hand, it also suggests that while sufficient F^{elec} can be quickly achieved due to the adequate negatively charged groups on surface, the uneven distribution of F^{elec} might be still present and some non-DLVO forces would take control of the particle growth over the DLVO forces. At c_{init} = 60 g/L, the shorter separation distance suppresses the exposure of surface ionizable group, and the original calibration point may be still applied, which is similar to that depicted in **Fig. 6a-d**. In all, it can be inferred that when lignin chains have sufficient F^{elec} leading to low collision efficiency and being meta-stable at a smaller size, the inherent heterogeneity of lignin can cause an uneven F^{elec} field. Besides, non-DLVO force can get involved, further complicating the particle growth. In the future work, incorporating heterogeneity of lignin as well as non-DLVO force in the energy calculations would be expected to increase the accuracy of the size prediction model.

4.4. Plausible aggregation patterns in LNP formation

The collision-driven aggregation toward LNP formation is mostly self-assembly under weak acid conditions as previously reported.[13, 14, 17, 19] The equilibrium of such an aggregation is a function of F^{vdW}, F^{elec}, and other interactions such as hydrophobic interactions and steric interactions. After mixing with an antisolvent, aggregation is initiated until sufficient repulsive force is reached, and the resulting particle sizes become stable. Based on the insights gained from this work, it becomes clear that colloidal dispersion forces, such as electrostatic and van der Waals interactions, are modulated by solution chemistry. The modulation ability is due to

the pK_a values of different functional groups and Hamaker constants of lignin. It should be noted that the factors such as the mixing rate for adding an antisolvent/agitating a mixture can also influence the final particle sizes and dispersity.[2, 3] In recent studies, the incorporation of shear force in theoretically calculation was proposed on classical spherical particles aggregation model, [52, 53] which can be subject of future study in polymer self-assembly. Nevertheless, the influence of mixing methods was taken into account in our size prediction model using appropriate calibration points, which were consistent across all the associated data points. Further investigations into dynamic fluidic properties would particularly elucidate mixing effect on particle sizes.

Overall, the size prediction can be performed by coupling the particle-particle interaction energy profile based on DLVO theory with the population balance model. Essentially, such DLVO force-driven aggregation pattern is favored by lignin that tends to be highly folded and hydrophobic core can be easily formed and stable. Ionizable functional group content and molecular weight distribution of lignin are two key intrinsic characteristics determining aggregation. The carboxyl groups in lignin mainly contribute to F^{elec} in particle-particle interactions (**Fig. S4**). From the energy perspective, the particles containing more ionizable groups like carboxyl groups can result in a deeper energy barrier even at a small size. However, we found that those functional group contents in lignin do not directly correlate with the particle-particle interaction forces. For example, OL with more carboxyl groups than KL and EKL, forms larger particle sizes. Similar observations were also reported in prior studies.[17, 31] The phenomena can be attributed to ionizable phenolic hydroxyl groups and molecular weight. Phenolic hydroxyl functional groups that are ionized at different degrees (**Fig. 1 and S2**) can potentially interrupt molecular interactions such as π-π stacking and hydrogen bonding interactions. In addition, lignin with high molecular weight can be easily self-aggregated due to steric hindrance, thus preferably forming into smaller particles (**Fig. 1c**). External factors

such as low pH and high salt concentration not only reduce the F^{elec} via the screening effect, but also maintain the folded structure of lignin by decreasing the dissociation degree of ionizable groups. On the other hand, a folded structure of lignin responds to the availability of ionizable groups on the surface, which eventually determines the repulsive energy barrier of particles. A high initial lignin concentration (corresponding to a close particle separation distance) would reduce the surface ionizable group density by increasing collision efficiency, thus resulting in large particle sizes.

For the underestimation in model-predicated data mostly found from weak base conditions or more hydrophilic lignin, the non-DLVO force and heterogeneous nature of lignin are believed to be the main causes. For example, the screening effect from NH_4^+ and HCO_3^- ions under weak base conditions cannot significantly determine the energetically equilibrated particle sizes. One reasonable explanation is strongly hydrophilic and/or hydrophobic interaction forces caused by structured water molecules. The ionizable functional groups can create the structured water molecules on the surface of LNPs. On one hand, steric repulsion could thus be generated due to strong solvent-surface interactions rather than solvent-solvent interactions.[54-56] on the other hand, the metastable water molecules results from the interactions between hydrophobic groups and water molecules and can further act as a bridge force between surfaces inducing strongly attractive surface interactions.[55, 57]

We proposed six assembly patterns of lignin chains based on different lignin structures (**Fig. 7**). Under a weak acid condition, lignin like KL with a good amphiphilic balance and relatively high molecular weight can form nanoparticles (**Route A**). Lignin like AKL with higher molecular weight reaches equilibrium at the smaller sizes than OL and EKL with less collision and attachments. lignin such as OL and EKL with smaller molecular weight or more hydrophobicity tends to grow into the large and irregular particles as more lignin chains attach on surfaces to reach sufficient repulsive forces and maintain stable surface ionizable group

densities (**Route B**). Under a weak-base condition, the deprotonation of both carboxyl groups and phenolic hydroxyl groups promotes the formation of more hydrophilic and negatively charged surfaces. KL was found hard to attach with more chains to form uniform particles at the average particle distance over 18.5 nm (c_{init} = 10 g/L) (**Fig. S6**) owing to the strong F^{elec} endowed by the ionized groups (**Route C**). By suppressing the extended structure upon the smaller average particle distance and lower pH, part of KL chains can assemble into particles again (**Route D**). The LNP synthesis of OL and EKL is favored under a weak base condition due to more ionizable groups exposed on lignin chain surfaces (**Route E**). However, the lignin attachments between small lignin chains might create cavities in a particle or easily lead to relatively larger sizes. The different aggregation pattern caused by different molecular weight and lignin structure was further observed in the LNP synthesis at c_{init} = 10 g/L and weak-base conditions. The morphology of AKL-, KL-, and EKL-NPs at the high c_{init} (= 60 g/L) is also observed via TEM (**Fig. 8**). It is clearly shown that KL-NPs had excess amorphous or small particles surrounding the surfaces due to the mixed Route C and D. AKL-NPs are mainly local clusters, representing Route C. The morphology of AKL-NPs is similar to the reported cationic LNP when 1,4-dioxane was the solvent and DI water was antisolvent.[58] For the EKL that mainly has low molecular weight fractions, the morphology looks similar to KL-NPs at the lower concentration and suggests the LNP formation follows Route E. The difference reflects the self-assembly patterns between large and small molecular weight fractions. While it brings a more negatively charged surface to the aggregated particles, non-DLVO forces get involved (**Route F**). It should be noted that Route F can occur at either moderately low or high pH range, but the effects on the final size vary depending on the portion of lignin chains engaged in this route. All those routes suggest DLVO forces, non-DLVO forces and/or possibly uneven collision efficiency between lignin chains can take part in the particle formation depending on amphiphilic balance of lignin and structural heterogeneity.

5. Conclusions

Our work demonstrated that the DLVO-force driven lignin chain collision-attachment model illustrates the lignin self-assembly from the perspective of interaction forces and predict the equilibrium size of lignin nanoparticles under various synthesis conditions. The application of the established DLVO-PBE model also allows us to propose a new lignin self-assembly mechanism which clarifies six aggregation patterns based on lignin molecular weight, ionizable functional groups, and driven forces of the aggregation. This work also suggests new strategies for regulating amphiphilic balance of lignin based on lignin structure and solution chemistry for size-tailorable nanoparticle synthesis.

ASSOCIATED CONTENT

Supporting Information

Supporting Information is available online or from the authors.

AUTHOR INFORMATION

Corresponding Author

* Corresponding authors. Tel: +1 573 884 8918; E-mail: j.lee@missouri.edu. Tel: +1 573 884 7882; E-mail: wanca@missouri.edu.

ORCID

Caixia Wan: 0000-0001-5490-7490

Author Contributions

The manuscript was written through contributions of all the authors. The authors have given approval to the final version of the manuscript.

Notes

The authors declare that they have no competing interests.

ACKNOWLEDGEMENTS

This work was in part supported by the USDA National Institute of Food and Agriculture (Award No. 2021-67021-34504).

References

1. X. Zhang, J. Zhang, H. Yang, C. He, Y. Ke, S. Singh and G. Cheng, *ChemSusChem*, 2022, **15**, e202201230.
2. J. Wang, W. Chen, D. Yang, Z. Fang, W. Liu, T. Xiang and X. Qiu, *Small*, 2022, **18**, 2200671.
3. A. Manisekaran, P. Grysan, B. Duez, D. F. Schmidt, D. Lenoble and J.-S. Thomann, *Journal of Colloid and Interface Science*, 2022, **626**, 178-192.
4. T. Pang, G. Wang, H. Sun, L. Wang, Q. Liu, W. Sui, A. M. Parvez and C. Si, *ACS Sustainable Chemistry & Engineering*, 2020, **8**, 9174-9183.
5. M. M. Cajnko, G. Sposito, Ž. Lavrič, A. Campisi, M. Grilc and B. Likozar, *Biomass Conversion and Biorefinery*, 2022.
6. M. H. Hussin, J. N. Appaturi, N. E. Poh, N. H. A. Latif, N. Brosse, I. Ziegler-Devin, H. Vahabi, F. A. Syamani, W. Fatriasari, N. N. Solihat, A. Karimah, A. H. Iswanto, S. H. Sekeri and M. N. M. Ibrahim, *International Journal of Biological Macromolecules*, 2022, **200**, 303-326.
7. J. Garg, M. Nee Chiu, S. Krishnan, L. Kumar Tripathi, S. Pandit, B. Farasati Far, N. Kumar Jha, K. Kumar Kesari, V. Tripathi, S. Pandey and P. Kumar Gupta, *Materials Letters*, 2022, **311**, 131573.
8. K. Chen, S. Wang, Y. Qi, H. Guo, Y. Guo and H. Li, *ChemSusChem*, 2021, **14**, 1284-1294.
9. I. F. Demuner, J. L. Colodette, A. J. Demuner and C. M. Jardim, *2019*, 2019, **14**, 39.
10. M. Ago, S. Huan, M. Borghei, J. Raula, E. I. Kauppinen and O. J. Rojas, *ACS Appl. Mater. Interfaces*, 2016, **8**, 23302.
11. A. P. Richter, B. Bharti, H. B. Armstrong, J. S. Brown, D. Plemmons, V. N. Paunov, S. D. Stoyanov and O. D. Velev, *Langmuir*, 2016, **32**, 6468.
12. Y. Qian, Y. Deng, X. Qiu, H. Li and D. Yang, *Green Chemistry*, 2014, **16**, 2156-2163.
13. J. D. Zwilling, X. Jiang, F. Zambrano, R. A. Venditti, H. Jameel, O. D. Velev, O. J. Rojas and R. Gonzalez, *Green Chemistry*, 2021, **23**, 1001-1012.
14. M. H. Sipponen, H. Lange, M. Ago and C. Crestini, *ACS Sustainable Chemistry & Engineering*, 2018, **6**, 9342-9351.
15. J. Deng, S.-F. Sun, E.-Q. Zhu, J. Yang, H.-Y. Yang, D.-W. Wang, M.-G. Ma and Z.-J. Shi, *Industrial Crops and Products*, 2021, **164**, 113412.
16. M. Österberg, M. H. Sipponen, B. D. Mattos and O. J. Rojas, *Green Chemistry*, 2020, **22**, 2712-2733.
17. I. V. Pylypchuk, A. Riazanova, M. E. Lindström and O. Sevastyanova, *Green Chemistry*, 2021, **23**, 3061-3072.
18. Z. Jiang, Y. Ma, X. Guo, J. Remón, D. C. W. Tsang, C. Hu and B. Shi, *Journal of Hazardous Materials*, 2021, **403**, 123701.

19. L. Chen, S.-M. Luo, C.-M. Huo, Y.-F. Shi, J. Feng, J.-Y. Zhu, W. Xue and X. Qiu, *Green Chemistry*, 2022, **24**, 285-294.
20. H. Li, Y. Deng, J. Liang, Y. Dai, B. Li, Y. Ren, X. Qiu and C. Li, *BioResources*, 2016, **11**, 11.
21. P. K. Mishra and A. Ekielski, *Nanomaterials*, 2019, **9**, 243.
22. M. Ma, L. Dai, J. Xu, Z. Liu and Y. Ni, *Green Chemistry*, 2020, **22**, 2011-2017.
23. N. T. K. Thanh, N. Maclean and S. Mahiddine, *Chemical Reviews*, 2014, **114**, 7610-7630.
24. E. Jasiukaitytė-Grojzdek, M. Huš, M. Grilc and B. Likozar, *Scientific Reports*, 2020, **10**, 11037.
25. E. M. Anderson, M. L. Stone, M. J. Hülsey, G. T. Beckham and Y. Román-Leshkov, *ACS Sustainable Chemistry & Engineering*, 2018, **6**, 7951-7959.
26. T. Ročnik, B. Likozar, E. Jasiukaitytė-Grojzdek and M. Grilc, *Chemical Engineering Journal*, 2022, **448**, 137309.
27. M. M. Cajnko, J. Oblak, M. Grilc and B. Likozar, *Bioresource Technology*, 2021, **340**, 125655.
28. I. V. Pylypchuk, P. A. Lindén, M. E. Lindström and O. Sevastyanova, *ACS Sustainable Chemistry & Engineering*, 2020, **8**, 13805-13812.
29. J. Y. Lee, Z. Shou and A. C. Balazs, *Macromolecules*, 2003, **36**, 7730-7739.
30. K. S. Shalaby, M. E. Soliman, L. Casettari, G. Bonacucina, M. Cespi, G. F. Palmieri, O. A. Sammour and A. A. El Shamy, *Int J Nanomedicine*, 2014, **9**, 4953-4964.
31. J. H. Lee, T. M. Kim, I.-G. Choi and J. W. Choi, *Nanomaterials*, 2021, **11**, 1790.
32. J. H. Lee, K. Kim, X. Jin, T. M. Kim, I.-G. Choi and J. W. Choi, *International Journal of Biological Macromolecules*, 2021, **183**, 660-667.
33. W. B. Russel, D. A. Saville and W. R. Schowalter, *Colloidal Dispersions*, Cambridge University Press, Cambridge, 1989.
34. R. Hollertz, H. Arwin, B. Faure, Y. Zhang, L. Bergström and L. Wågberg, *Cellulose*, 2013, **20**, 1639-1648.
35. M. Norgren, H. Edlund and L. Wågberg, *Langmuir*, 2002, **18**, 2859-2865.
36. A. K. Atmuri, M. A. Henson and S. R. Bhatia, *Colloids and Surfaces A: Physicochemical and Engineering Aspects*, 2013, **436**, 325-332.
37. D. Zhang, Q. Li and V. Prigiobbe, *Chemical Engineering Science*, 2022, **247**, 117035.
38. A. Chaturbedi, C. Pathak, K. Deshpande, N. Shapley and R. Ramachandran, *Chemical Engineering Research and Design*, 2016, **113**, 96-111.
39. J. N. Israelachvili, in *Intermolecular and Surface Forces (Third Edition)*, ed. J. N. Israelachvili, Academic Press, San Diego, 2011, pp. 253-289.
40. J. N. Israelachvili, in *Intermolecular and Surface Forces (Third Edition)*, ed. J. N. Israelachvili, Academic Press, San Diego, 2011, pp. 291-340.
41. B. W. Ninham and V. A. Parsegian, *Journal of Theoretical Biology*, 1971, **31**, 405-428.
42. S. Bhattacharjee, M. Elimelech and M. Borkovec, *Croatica Chemica Acta*, 1998, **71**, 883-903.
43. L. Liang, Y. Wang and Z. Pan, *Particuology*, 2016, **25**, 83-92.
44. F. H. B. Sosa, A. Bjelić, J. A. P. Coutinho, M. C. Costa, B. Likozar, E. Jasiukaitytė-Grojzdek, M. Grilc and A. M. da Costa Lopes, *Sustainable Energy & Fuels*, 2022, **6**, 4800-4815.
45. M. Ragnar, C. T. Lindgren and N.-O. Nilvebrant, *Journal of Wood Chemistry and Technology*, 2000, **20**, 277-305.
46. E. Lizundia, M. H. Sipponen, L. G. Greca, M. Balakshin, B. L. Tardy, O. J. Rojas and D. Puglia, *Green Chemistry*, 2021, **23**, 6698-6760.
47. W. Zhang, in *Nanomaterial: Impacts on Cell Biology and Medicine*, eds. D. G. Capco

and Y. Chen, Springer Netherlands, Dordrecht, 2014, pp. 19-43.
48. M. Norgren and B. Lindström, 2000, **54**, 519-527.
49. N. Jahan, M. M. Huda, Q. X. Tran and N. Rai, *The Journal of Physical Chemistry B*, 2022, **126**, 5752-5764.
50. C. Cui, R. Sun and D. S. Argyropoulos, *ACS Sustainable Chemistry & Engineering*, 2014, **2**, 959-968.
51. G. Zinovyev, I. Sumerskii, P. Korntner, I. Sulaeva, T. Rosenau and A. Potthast, *Journal of Wood Chemistry and Technology*, 2017, **37**, 171-183.
52. V. Bal, *Journal of Colloid and Interface Science*, 2020, **564**, 170-181.
53. J. Gao, T. Sugimoto and M. Kobayashi, *Journal of Colloid and Interface Science*, 2023, **638**, 733-742.
54. Y. Zhu and S. Granick, *Langmuir*, 2003, **19**, 8148-8151.
55. S. H. Donaldson Jr, A. Røyne, K. Kristiansen, M. V. Rapp, S. Das, M. A. Gebbie, D. W. Lee, P. Stock, M. Valtiner and J. Israelachvili, *Langmuir*, 2015, **31**, 2051-2064.
56. J. Lee, E. Nakouzi, D. Xiao, Z. Wu, M. Song, C. Ophus, J. Chun and D. Li, *Small*, 2019, 1901966.
57. X. Zhang, Y. Zhu and S. Granick, *Science*, 2002, **295**, 663-666.
58. D. Liu, J. Liu, Y. Zhou, J. Chen, P. Zhan, G. Yang and Z. Wu, *RSC Advances*, 2020, **10**, 18594-18600.

Figure captions

Fig. 1 (a) Phenolic hydroxyl group contents determined by UV difference method and ^{31}P NMR. (b) Ionized phenolic groups of KL, OL, and EKL in 20 mM NH_4HCO_3. (c) LNP size and Đ as the function of molecular weight when DI water as antisolvent and c_{init} = 10 g/L.

Fig. 2 Schematic depiction of the key factors in both LNP synthesis and the particle-particle interaction force calculation.

Fig. 3 TEM images. (a) KL-NPs with c_{init} = 10 g/L and DI water as antisolvent and (b) KL-NPs with c_{init} =30 g/L and 20 mM NH_4HCO_3 as antisolvent. (c) OL-NPs and (d) EKL-NPs with c_{init} = 10 g/L and 20 mM NH_4HCO_3 as antisolvent. Scale bar: 200 nm in the main images and 50 nm in the inset of (c).

Fig. 4 KL-NP size (a) as the function of $D_{average}$ /κ (or initial lignin concentration) at 10 mM NH_4Cl as antisolvent, (b) as the function of Debye length κ (or NH_4Cl concentration) at c_{init} = 10 g/L, (c) at the selected NH_4HCO_3 concentration with c_{init} = 10 g/L, and (d) as the function of $D_{average}$ /κ (or c_{init}) at 20 mM NH_4HCO_3 as antisolvent. (e) OL- and EKL-NP sizes and Đ as the function of c_{init} at 20 mM NH_4HCO_3 as antisolvent. Two points highlighted in the cyan circle are the LNPs synthesized in DI water as antisolvent for comparison. (f) ζ potential of KL-, OL-, EKL-NPs synthesized at 20 mM NH_4HCO_3 as antisolvent.

Fig. 5 (a) Energy barrier when a sphere with the radius of 24 nm interacts with a sphere 1 to 5 times larger. (b) Energy barrier between two identical spheres at pH 5.3 and 0.1 mM monovalent salt. (c) Brownian motion of spherical particles with the radius of 24 nm. (d) DLVO forces between two identical spheres with the radius of 24 nm at pH 5.3 and 0.1 mM monovalent salt.

Fig. 6 Predicted and measured LNP sizes at pH 2.97-5.25 for (a) KL-NPs and (b) OL-NPs, and at pH 7.44-8.48 for (c) KL-NPs and (d) OL-NPs. The calibration point is marked as red asterisk. (e) AKL-NP size distribution at different c_{init} with 20 mM NH_4HCO_3 as antisolvent. (f) Predicted LNP sizes compared with the 1st peak of AKL-NP size distribution (calibration point from (b) used).

Fig. 7 Proposed mechanism of lignin self-assembly at different pH and with various lignin structures. Six proposed lignin assembly patterns (A-F) (marked in the gray circles).

Fig. 8 TEM images of (a) KL-NPs, (b) AKL-NPs, and (c) EKL-NPs at c_{init} = 60 g/L and 20 mM NH_4HCO_3 as antisolvent.

Table 1 Functional group contents and molecular weights of technical lignin.

Lignin[*]	**KL**	**EKL**	**OL**
Aliphatic OH (mmol/g)	1.81	1.60	1.79
Carboxylic (mmol/g)	0.35	0.48	0.49
Total phenolic OH (mmol/g)	4.71	4.04	2.74
M_w (g/mol)	5529	2705	4055
M_w/M_n	3.10	2.15	2.77

[*] KL: kraft lignin; EKL: 95% ethanol soluble kraft lignin; OL: organosolv lignin. Functional group contents determined by ^{31}P NMR; Mw: weight average molecular weight; Mn: number average molecular weight.

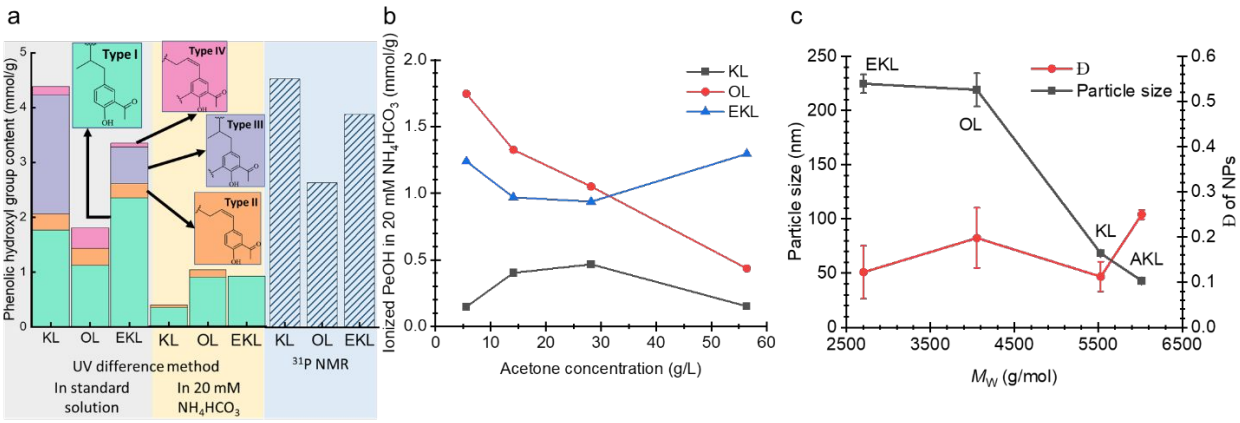

Fig. 1 (a) Phenolic hydroxyl group contents determined by UV difference method and ^{31}P NMR. (b) Ionized phenolic groups of KL, OL, and EKL in 20 mM NH_4HCO_3. (c) LNP sizes and Đ as the function of molecular weight when DI water as antisolvent and c_{init} = 10 g/L.

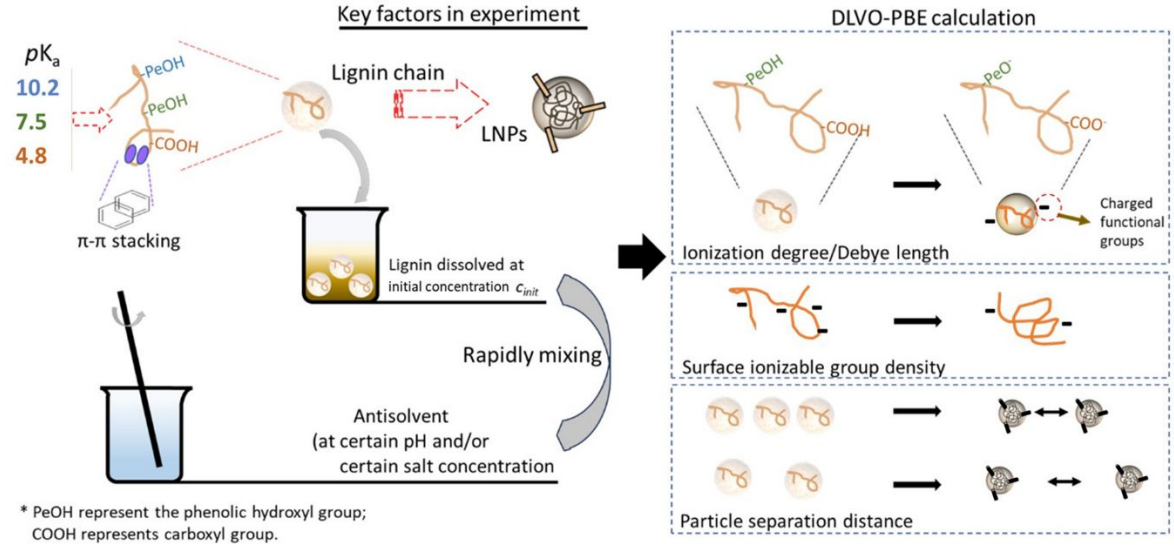

Fig. 2 Schematic depiction of the key factors in both LNP synthesis and the particle-particle interaction force calculation.

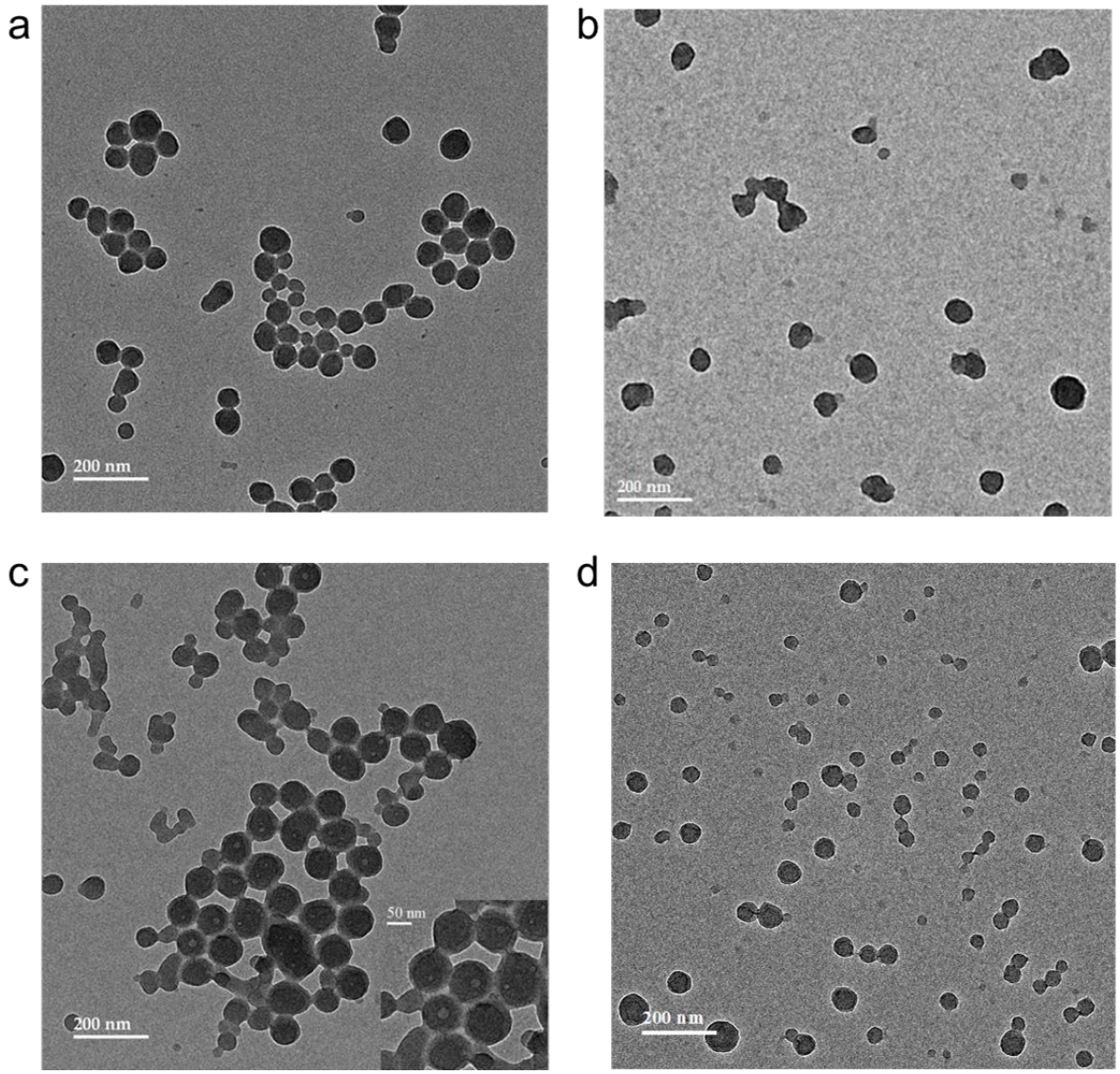

Fig. 3 TEM images. (a) KL-NPs with c_{init} = 10 g/L and DI water as antisolvent and (b) KL-NPs with c_{init} =30 g/L and 20 mM NH_4HCO_3 as antisolvent. (c) OL-NPs and (d) EKL-NPs with c_{init} = 10 g/L and 20 mM NH_4HCO_3 as antisolvent. Scale bar: 200 nm in the main images and 50 nm in the inset of (c).

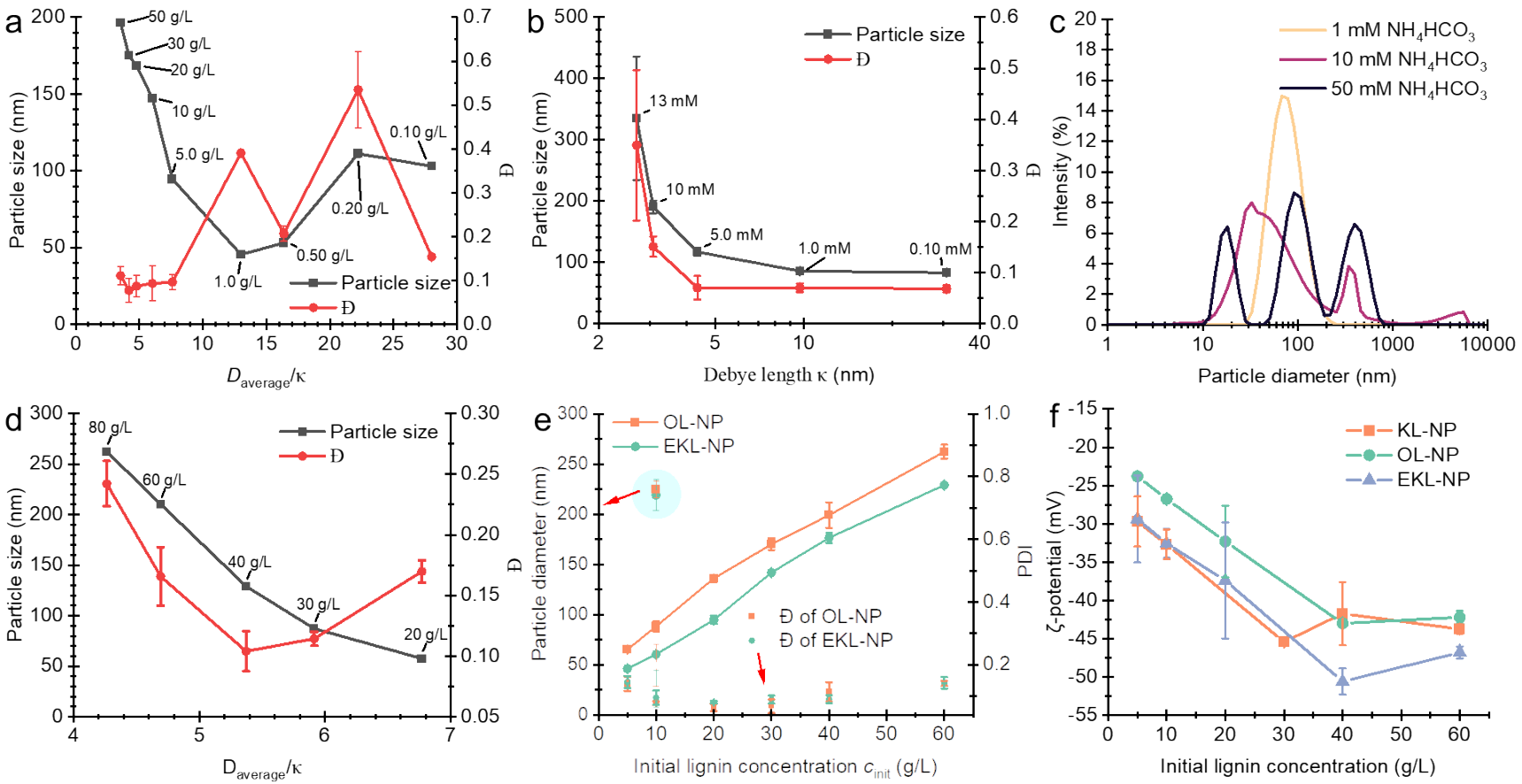

Fig. 4 KL-NP size (a) as the function of $D_{average}$ /κ (or initial lignin concentration) at 10 mM NH_4Cl as antisolvent, (b) as the function of Debye length κ (or NH_4Cl concentration) at c_{init} = 10 g/L, (c) at the selected NH_4HCO_3 concentration with c_{init} = 10 g/L, and (d) as the function of $D_{average}$ /κ (or c_{init}) at 20 mM NH_4HCO_3 as antisolvent. (e) OL- and EKL-NP sizes and Đ as the function of c_{init} at 20 mM NH_4HCO_3 as antisolvent. Two points highlighted in the cyan circle are LNPs synthesized in DI water as antisolvent for comparison. (f) ζ potential of KL-, OL-, EKL-NPs synthesized at 20 mM NH_4HCO_3 as antisolvent.

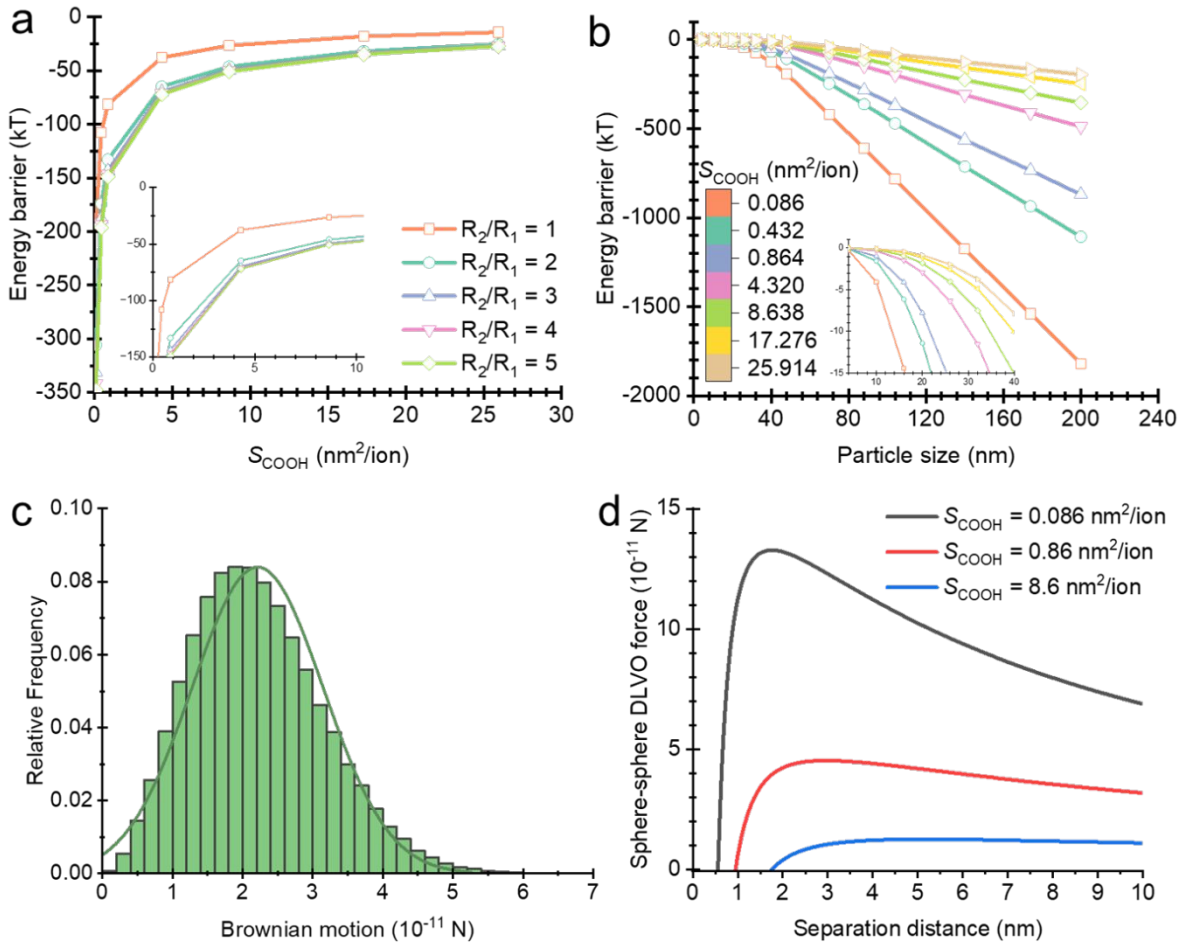

Fig. 5 (a) Energy barrier when a sphere with the radius of 24 nm interacts with a sphere 1 to 5 times larger. (b) Energy barrier between two identical spheres at pH 5.3 and 0.1 mM monovalent salt. (c) Brownian motion of spherical particles with the radius of 24 nm. (d) DLVO forces between two identical spheres with the radius of 24 nm at pH 5.3 and 0.1 mM monovalent salt.

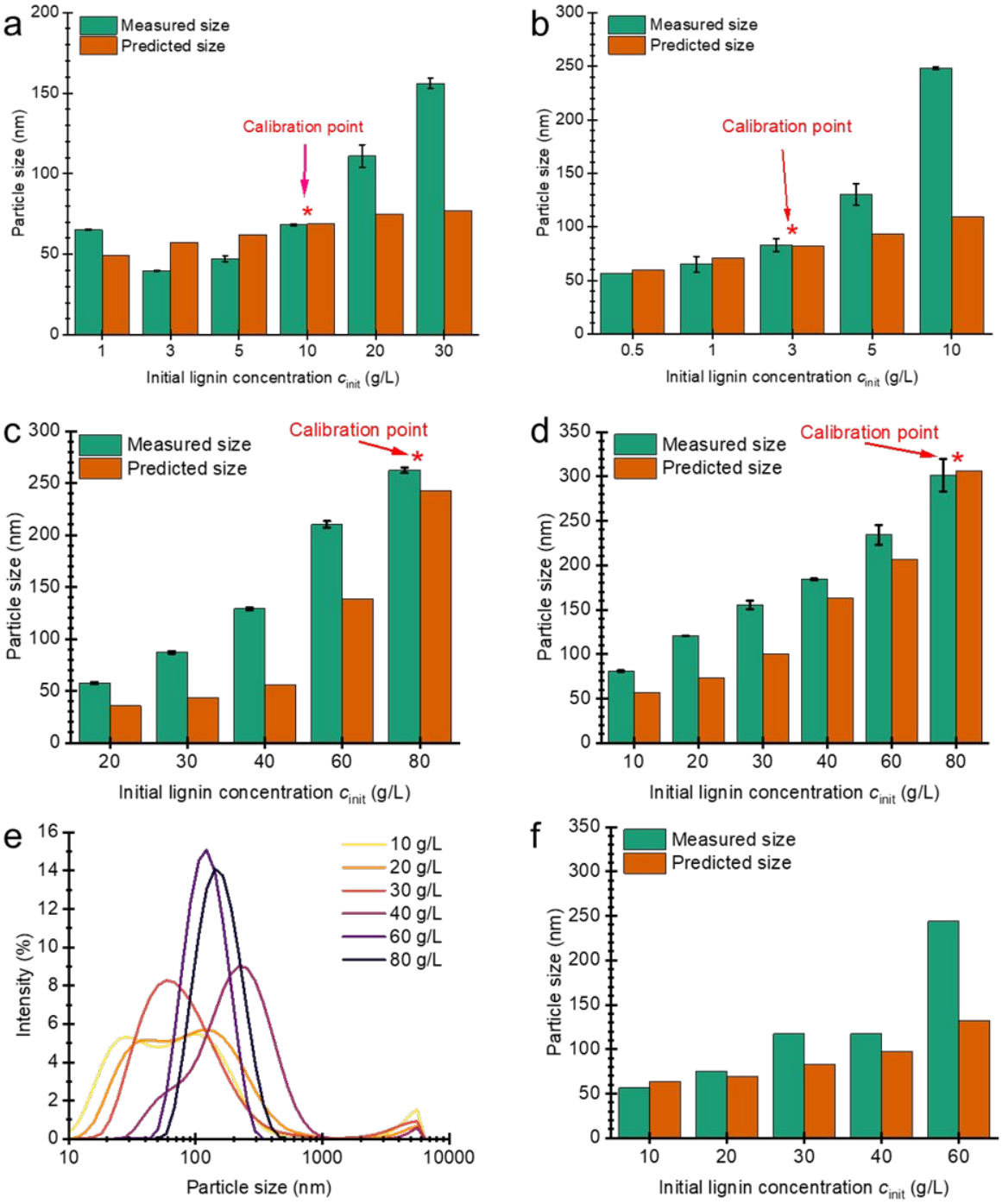

Fig. 6 Predicted and measured LNP sizes at pH 2.97-5.25 for (a) KL-NPs and (b) OL-NPs, and at pH 7.44-8.48 for (c) KL-NPs and (d) OL-NPs. The calibration point is marked as red asterisk. (e) AKL-NP size distribution at different cinit with 20 mM NH4HCO3 as antisolvent. (f) Predicted LNP sizes compared with the 1st peak of AKL-NP size distribution (calibration point from (b) used).

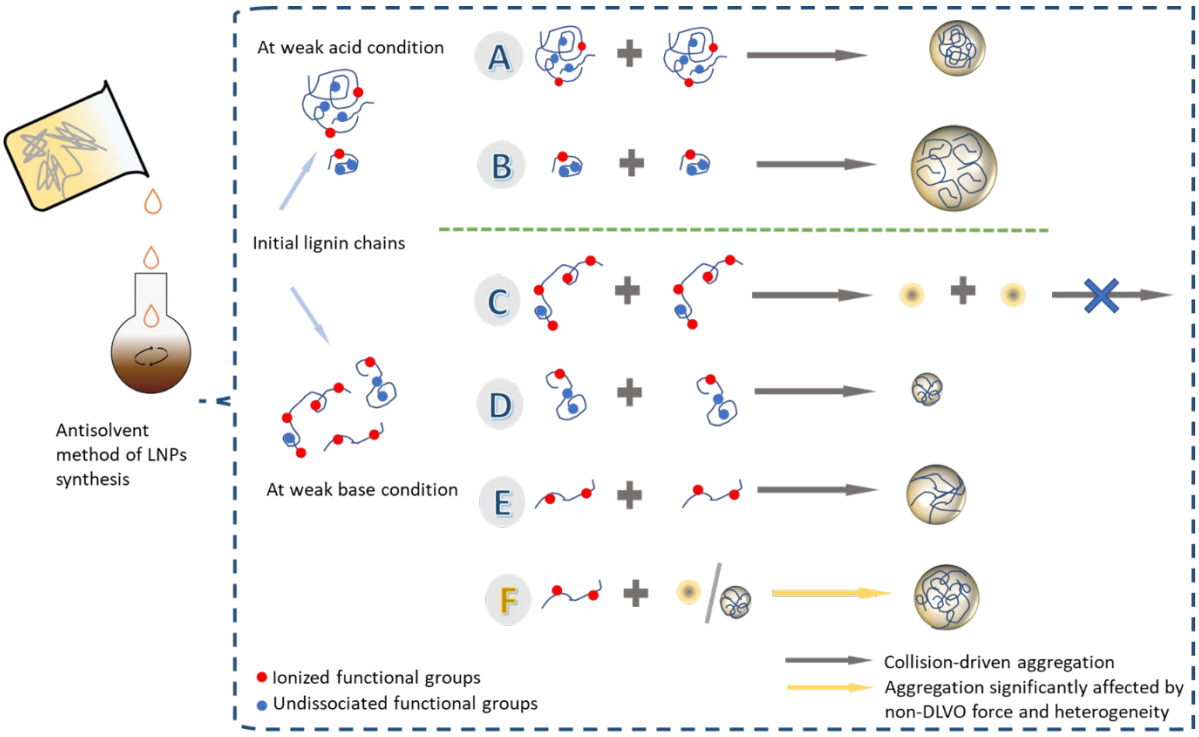

Fig. 7 Proposed mechanism of lignin self-assembly at different pH and with various lignin structures. Six proposed lignin assembly patterns (A-F) (marked in the gray circles).

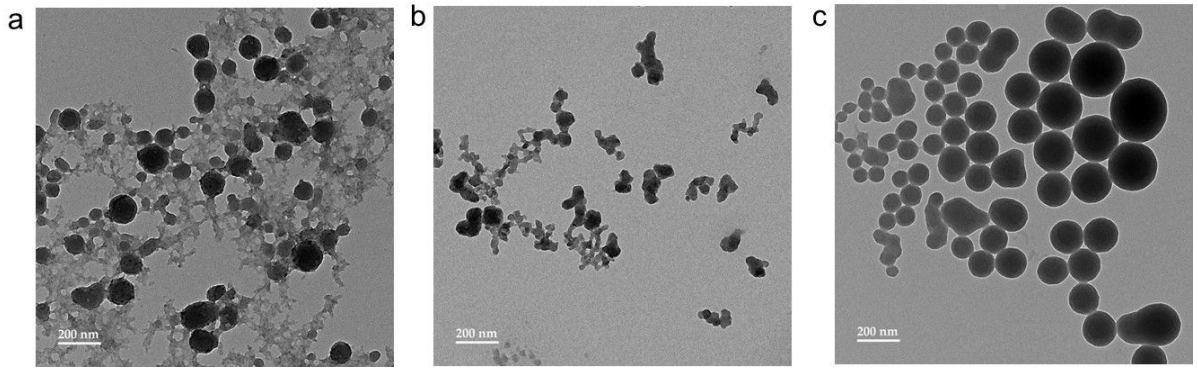

Fig. 8 TEM images of (a) KL-NPs, (b) AKL-NPs, and (c) EKL-NPs at c_{init} = 60 g/L and 20 mM NH4HCO3 as antisolvent.